

RESEARCH ARTICLE

10.1002/2016JA023777

Special Section:

Magnetospheric Multiscale (MMS) mission results throughout the first primary mission phase

Key Points:

- Interior fine structures of two ion-scale flux ropes are resolved for which some of their flux rope properties are contrasted
- Crater is formed within one flux rope where magnetic pressure decreases while thermal pressure increases
- Crater formation can be interpreted by flux rope simulation as evolution of typical flux rope to crater-like one due to pressure increase

Correspondence to:

W.-L. Teh,
waleong.teh@gmail.com

Citation:

Teh, W.-L., et al. (2017), Evolution of a typical ion-scale magnetic flux rope caused by thermal pressure enhancement, *J. Geophys. Res. Space Physics*, 122, 2040–2050, doi:10.1002/2016JA023777.

Received 5 DEC 2016

Accepted 13 FEB 2017

Accepted article online 18 FEB 2017

Published online 28 FEB 2017

Evolution of a typical ion-scale magnetic flux rope caused by thermal pressure enhancement

W.-L. Teh¹ , T. K. M. Nakamura² , R. Nakamura² , W. Baumjohann² , C. T. Russell³ , C. Pollock⁴ , P.-A. Lindqvist⁵ , R. E. Ergun⁶ , J. L. Burch⁷ , R. B. Torbert^{7,8} , and B. L. Giles⁹ 
¹Space Science Centre, Institute of Climate Change, Universiti Kebangsaan Malaysia, Bangi, Malaysia, ²Space Research Institute, Austrian Academy of Sciences, Graz, Austria, ³Department of Earth, Planetary and Space Sciences, University of California, Los Angeles, California, USA, ⁴Denali Scientific, Healy, Alaska, USA, ⁵School of Electrical Engineering, Royal Institute of Technology, Stockholm, Sweden, ⁶Laboratory for Atmospheric and Space Physics, University of Colorado Boulder, Boulder, Colorado, USA, ⁷Southwest Research Institute, San Antonio, Texas, USA, ⁸Space Science Center, University of New Hampshire, Durham, New Hampshire, USA, ⁹NASA Goddard Space Flight Center, Green Belt, Maryland, USA

Abstract With high time-resolution field and plasma measurements by the Magnetospheric Multiscale spacecraft, interior fine structures of two ion-scale magnetic flux ropes (~5 and ~11 ion inertial length radius) separated by ~14 s are resolved. These two ion-scale flux ropes (FR1 and FR2) show non-frozen-in ion behavior and consist of a strong axial magnetic field at the reversal of the negative-then-positive bipolar field component. The negative bipolar field component of the FR2 is found to be depressed, where magnetic pressure and total pressure decrease, but ion and electron thermal pressures increase, a feature akin to a crater-like flux rope. The pressure enhancement is due to the magnetosheath plasma feeding into the flux rope along the field lines. Magnetic field draping and energetic electrons are also observed in the trailing part of the FR2. The ratio of perpendicular and parallel currents indicates that the FR1 appears force-free but the FR2 seems not. Moreover, the FR2 is time-dependent as a result of a low correlation coefficient ($CC = 0.75$) for the derivation of the deHoffmann-Teller frame using the direct measured electric fields, while the FR1 is in quasi-steady conditions ($CC = 0.94$). It is concluded that the crater formation within the FR2 can be interpreted by the analytical flux rope simulation as the evolution of typical flux rope to crater-like one due to the thermal pressure enhancement, which could be induced by the depression of transverse magnetic fields of the flux rope.

1. Introduction

Magnetic flux ropes are of a helical magnetic field structure with an axial field at the flux rope center. This helical field structure is of great interest to studying magnetic reconnection in the terrestrial magnetosphere and also on the Sun, because it is a by-product of magnetic reconnection [e.g., Teh et al., 2014; Wang et al., 2016]. Magnetic flux ropes at the magnetopause can be classified into the typical and crater-like flux rope [e.g., Paschmann et al., 1982; Farrugia et al., 1988; Zhang et al., 2010; Teh et al., 2015]. The former has a magnetic pressure peak at the flux rope center, while the latter has a dip instead. Recently, Teh et al. [2015] have shown that the formation of a crater-like flux rope can be evolved from a typical one and vice versa.

On 12 March 2015, four Magnetospheric Multiscale (MMS) spacecraft with high time-resolution scientific instruments onboard were launched into space for exploring the microphysics of magnetic reconnection in the small-scale electron diffusion region [Burch et al., 2016]. With the high time-resolution measurements of fields and particles, new MMS findings have been reported recently for observations of magnetic flux ropes at the dayside magnetopause and in the magnetosheath. Eastwood et al. [2016] have identified the non-frozen-in ion behavior within the ion-scale flux ropes. Using the ratio of perpendicular current to parallel current, Farrugia et al. [2016] have identified the non-force-free state of the flux rope embedded within a super-Alfvénic flow. Hwang et al. [2016] have shown the substructures of the flux rope and the magnetic connectivity inside and surrounding the flux rope. Zhao et al. [2016] have calculated the magnetic and pressure forces to demonstrate the non-force-free magnetic flux ropes at the magnetopause.

In this paper, new MMS findings for the ion-scale flux ropes are reported. Two ion-scale flux ropes separated by ~14 s are found in the magnetosheath after the inbound magnetopause crossing for which some properties of these two flux ropes are contrasted. One appears to be in quasi-steady state and force-free state, while the other one (FR2) seems not. For FR2, its interior fine structures of magnetic and thermal pressures reveal

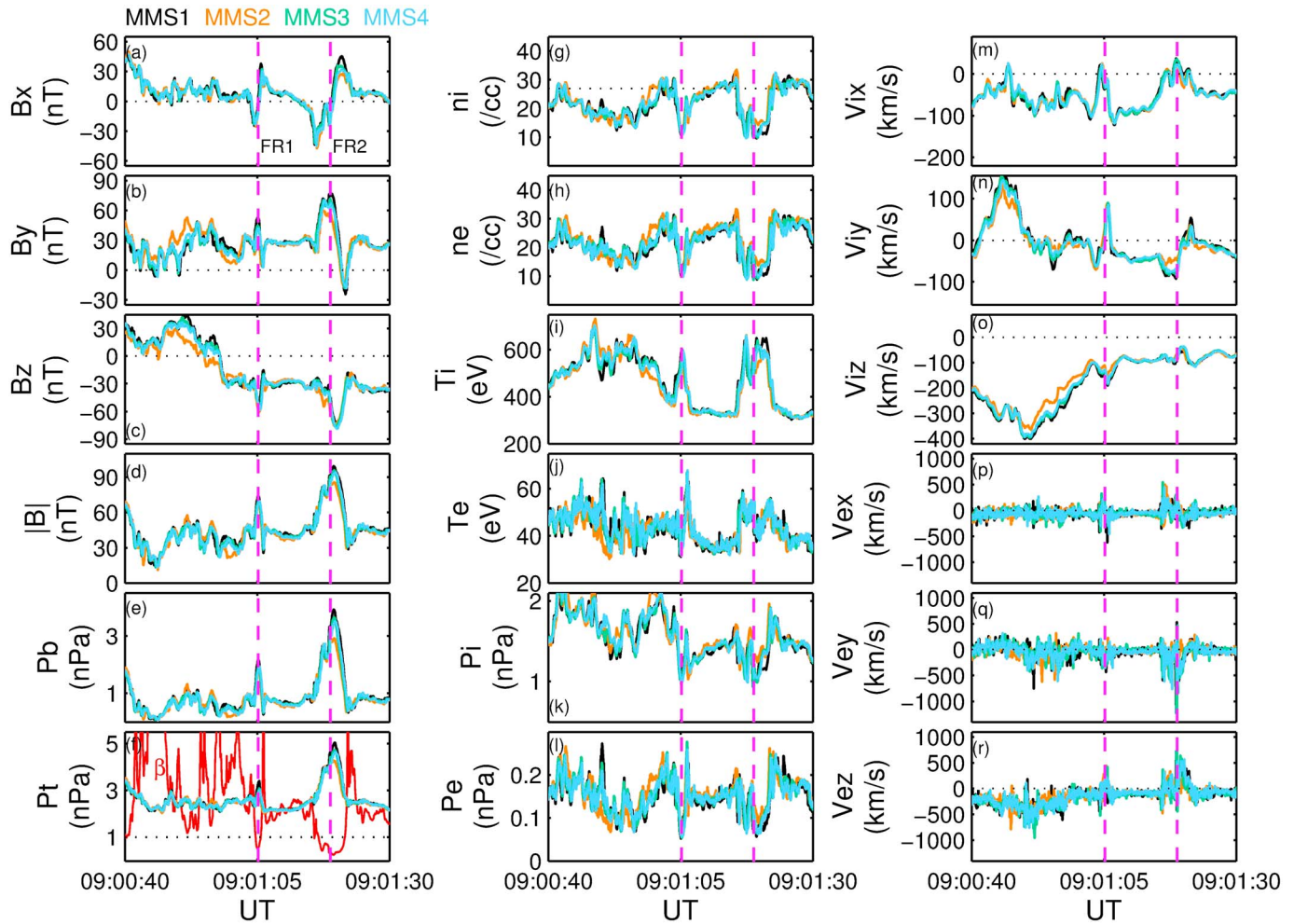


Figure 1. MMS observations of two magnetic flux ropes in the interval 09:00:40 UT–09:01:30 UT, on 10 January 2016. The data shown are magnetic field (B), ion and electron plasma density (n), temperature (T), velocity (V), and pressure (P). The subscripts i and e denote ion and electron. Vectors are in GSE. The total pressure P_t is a sum of magnetic pressure P_b , and ion and electron pressures. The plasma beta, $(P_i + P_e)/P_b$, is shown in red for MMS1 in Figure 1f. The two vertical magenta dashed lines mark the center of the two flux ropes.

that the flux rope is evolving. Furthermore, magnetic field draping and energetic electrons are found in the trailing part of the flux rope. This paper is organized as follows. In section 2, an overview of MMS observations of the two flux ropes is present. In section 3, the parallel and perpendicular currents of the flux rope is examined. In section 4, we demonstrate the non-frozen-in ion behavior of the flux rope and perform the deHoffmann-Teller frame analysis to investigate the steady conditions. In section 5, we perform a flux rope simulation to interpret the observations. Finally, summary and discussion are given in section 6.

2. MMS Observations

Between 09:01:00 UT and 09:01:30 UT, on 10 January 2016, MMS observations of two magnetic flux ropes were made in the magnetosheath after the inbound magnetopause crossing at 09:00:58 UT around $(8.9, -2.6, -0.8) R_E$ (the Earth's radius) in geocentric solar ecliptic (GSE) coordinates. The mean distance of the MMS tetrahedron configuration is ~ 40 km, with a large distance of ~ 55 km between MMS1 and MMS2 and a small distance of ~ 24 km between MMS3 and MMS4.

Figure 1 shows measurements of fluxgate magnetometer (FGM) [Russell et al., 2016] and fast plasma experiment (FPI) [Pollock et al., 2016] in GSE for all four MMS spacecraft in the interval between 09:00:40 UT and 09:01:30 UT. The FGM data are at ~ 63 ms time resolution, and the FPI data for electron and ion are at 30 ms and 150 ms resolution, respectively. The color codes for MMS1–MMS4 are black, orange, green, and

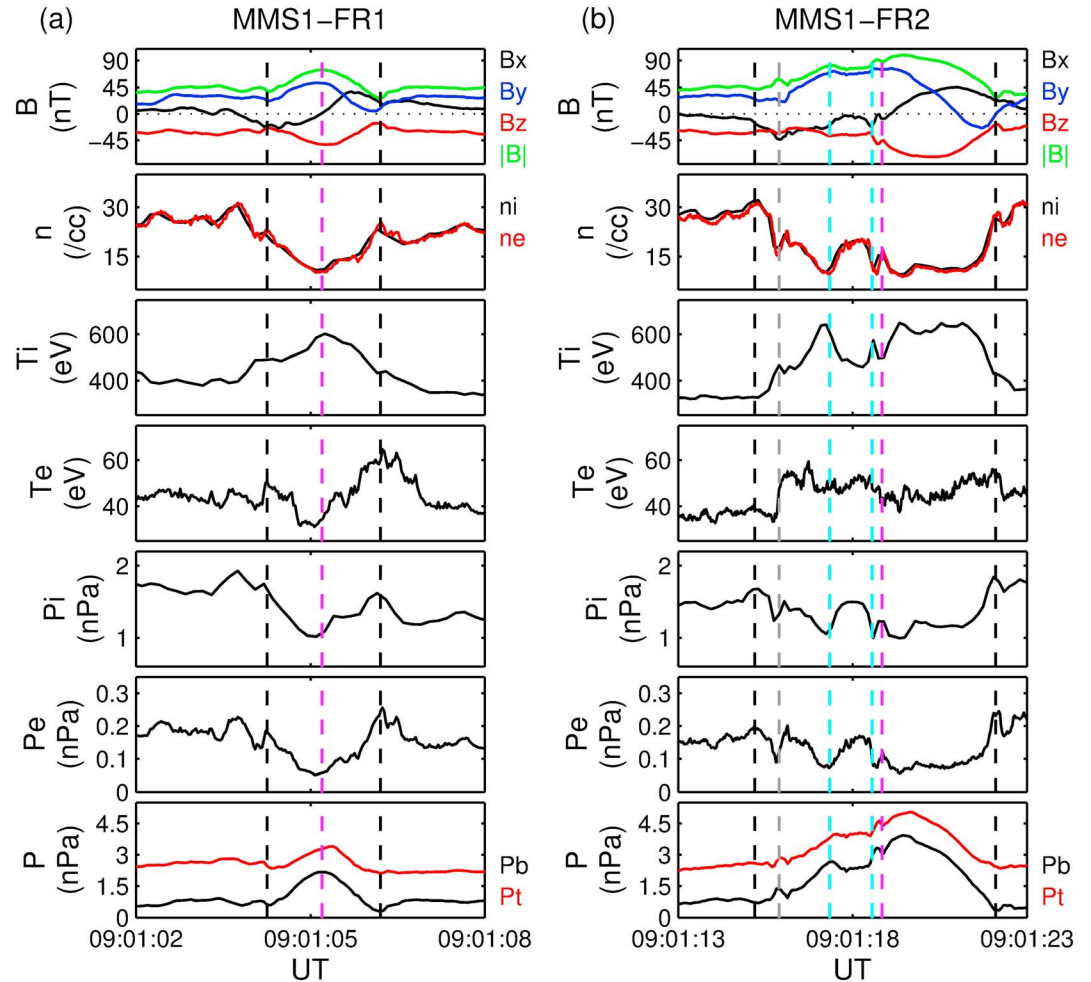


Figure 2. MMS1 observations of magnetic field and ion and electron plasmas for (a) FR1 and (b) FR2. The black and magenta dashed lines denote the flux rope interval and the flux rope center, respectively. The gray and cyan dashed lines mark the magnetic pressure increase and decrease, respectively.

blue, respectively. In Figure 1f, the total pressure P_t is a sum of magnetic pressure P_b and ion and electron thermal pressures (P_i and P_e). During the magnetopause crossing, a southward reconnection jet is observed as shown in Figure 1o. The magnetopause boundary coordinates are approximately seen as the GSE coordinates, where the x axis is expressed as the normal orientation of the magnetopause current layer. As indicated by the two vertical magenta dashed lines in Figure 1, the two magnetic flux ropes separated by ~ 14 s are identified by the negative-then-positive bipolar B_x field component and the field enhancement at the reversal of the bipolar signature. It is seen that the axial field of the two flux ropes has major components along the duskward and southward directions. The plasma density and thermal pressure for ion and electron are lower inside the flux rope as compared to the surrounding regions, a typical feature of magnetosheath flux ropes [e.g., Farrugia et al., 2016]. In Figure 1f, the plasma beta, $\beta = (P_i + P_e)/P_b$, is shown for MMS1 and is less than one within the flux rope.

Using four-spacecraft timing analysis [Schwartz, 1998] and the bipolar signatures, the first flux rope (FR1) moves with a speed of 118 km/s along $\mathbf{k}_1 = (0.024, -0.707, -0.707)$ GSE and the second flux rope (FR2) moves with a speed of 72 km/s along $\mathbf{k}_2 = (-0.025, -0.547, -0.836)$ GSE. Note that a consistent result is obtained if using the field strength instead for timing analysis. The southward motion of these two flux ropes is consistent with the sense of the bipolar signature. The durations of FR1 and FR2 are ~ 2.0 s and ~ 6.9 s, respectively, which correspond to the radii of ~ 236 km ($\sim 5 d_i$) and ~ 497 km ($\sim 11 d_i$) for FR1 and FR2, respectively. Here $d_i = 44$ km is the ion inertial length, which is calculated by using the magnetosheath density of 27 cm^{-3} . The FR2 is about 2 times larger in size than the FR1.

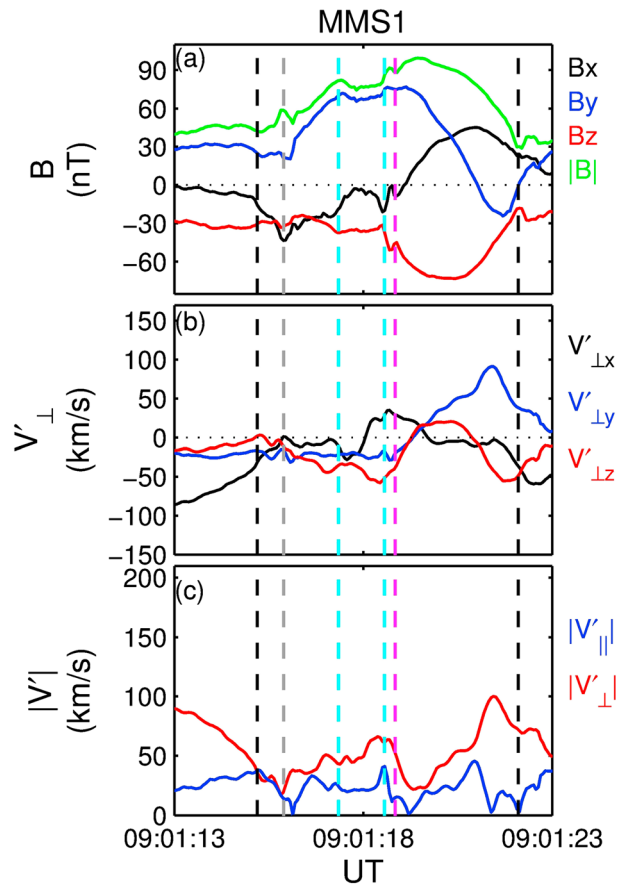


Figure 3. MMS1 observations of the magnetic field draping in the trailing part of the FR2. From top to bottom, shown are (a) magnetic fields, (b) perpendicular flows to the magnetic field in the moving frame with the FR2, and (c) the magnitude of the parallel and perpendicular flows. The dashed lines are the same as Figure 2b.

in the B_x between the second cyan dashed line and the magenta dashed line in Figure 2b. This feature is caused by the depression of B_x over the regions marked by the two cyan lines and the magenta line, where the thermal pressure is enhanced. The thermal pressure enhancement is due to the plasma density increase, which is the consequence of the magnetosheath plasma feeding into the flux rope along the field lines. These observations will be shown later.

In the trailing part of the FR2, the magnetic pressure is enhanced as a result of the enhancement of B_x and B_z field components as shown in Figure 3a. Figure 3b shows the perpendicular plasma flows to the magnetic field in the frame moving with the FR2. It is found that the y and z components of the perpendicular flows are enhanced around the trailing part of the FR2. Note that the trailing $V'_{\perp y}$ is not aligned with the flux rope motion because the flows are diverted around the obstacle. Also, Figure 3c shows that the magnitude of the perpendicular flow is increasing toward the trailing edge, while it is decreasing toward the leading edge. This result indicates that the magnetic field enhancement at the trailing edge of the FR2 is likely caused by the magnetic field draping [e.g., Farrugia *et al.*, 2016], for which the magnetic fields are accumulating and draping around an obstacle where the perpendicular flows are enhanced. Similar perpendicular flow pattern is also seen for the FR1, as shown in Figure 4. However, the magnetic field draping is not pronounced at the trailing part of the FR1, probably because the size of the FR1 is small such that its radius of curvature is small.

Figure 5a shows the electron pitch angle distribution for three different energy ranges for FR2. The electrons within the flux rope are dominant by the low-energy cold electrons (0–200 eV) from the magnetosheath. In the trailing part of the flux rope, the energetic electrons (2 k–30 k eV) are observed which could be resulted from the magnetic field draping. In the energy range of 200–2 k eV, these hot electrons within the flux

Figure 2a shows MMS1 observations of magnetic field and ion and electron plasma moments for FR1 in the interval between 09:01:02 UT and 09:01:08 UT. In the figure, the black and magenta vertical dashed lines denote the flux rope interval (09:01:4.25 UT–09:01:6.2 UT) and the flux rope center, respectively. It is seen that the FR1 is of a typical magnetic flux rope where the magnetic pressure peak is at the flux rope center. Figure 2b is the same format as Figure 2a, but for FR2. The FR2 interval is between 09:01:15.2 UT and 09:01:22.1 UT. Near the leading edge of the flux rope, it is found that the magnetic pressure increases but the thermal pressure decreases, as shown by the gray vertical dashed line. Apart from the flux rope center, there is a region, as marked by the two cyan dashed lines in Figure 2b, where (1) the magnetic pressure and total pressure decrease but the ion and electron thermal pressures enhance and (2) the strength of the B_x field component decreases. The first feature is akin to a crater-like flux rope. One can also find such a feature near the flux rope center, as indicated by the magenta dashed line. Note that there is a short bipolar feature

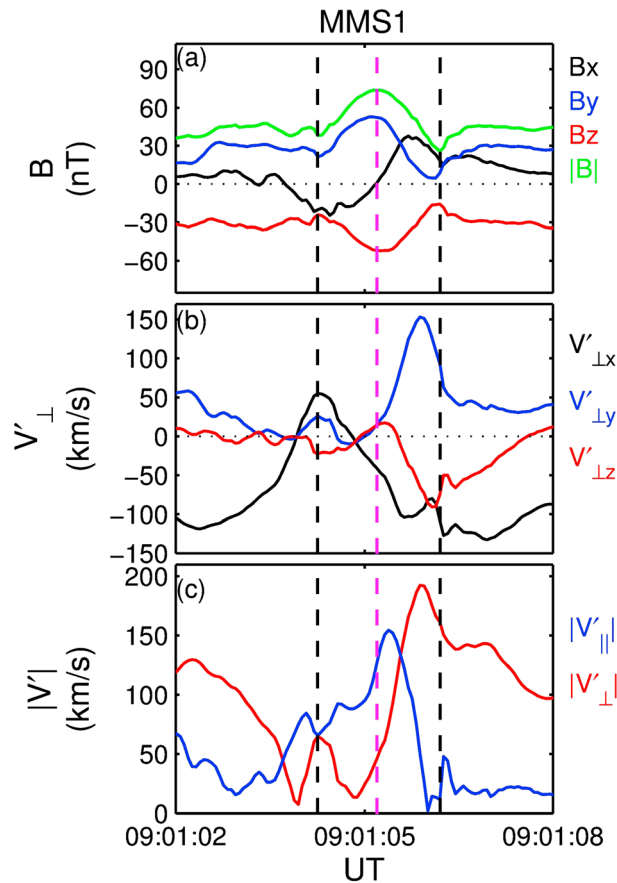


Figure 4. The same format as Figure 3 but for FR1.

rope are probably from the Earth's magnetosphere and the field-aligned electrons are seen at pitch angle $<30^\circ$, suggesting that the one end of the flux rope could be connected to the magnetic field of the Southern Hemisphere. The other end of the flux rope could thus be open to the magnetosheath. Inside the crater region as enclosed by the two cyan dashed lines, the field-aligned electrons at pitch angle $>150^\circ$ are enhanced, suggesting that the magnetosheath plasma is feeding into that region along the field lines, and thus, it enhances the thermal pressure. Note that the field-aligned ions at pitch angle $>150^\circ$ are also increased within the crater region (not shown). Figure 5b is the same format as Figure 5a, but for FR1. It is found that the magnetosheath plasma entry and the energetic electrons are not observed within the FR1. This result supports the observed differences between the two flux ropes. Note that the one end of the FR1 might also be connected to the Southern Hemisphere.

3. Parallel and Perpendicular Current of the Flux Rope

Figures 6 and 7 show the parallel and perpendicular currents and the current ratio for FR1 and FR2, respectively. The current density is calculated as $\mathbf{j} = qn_e(\mathbf{V}_i - \mathbf{V}_e)$, where n_e is the electron density, q is the electron charge, and \mathbf{V}_i and \mathbf{V}_e are the proton and electron velocity. Note that the electric current is mainly carried by electrons for these two flux ropes. In force-free conditions, i.e., $\mathbf{j} \times \mathbf{B} = 0$, the perpendicular current \mathbf{j}_\perp is zero. Therefore, the ratio $\alpha = j_\perp/j_\parallel$ can be used as a proxy for inspecting the force-free conditions ($\alpha < 1$) [Farrugia et al., 2016]. Figure 6 indicates that the FR1 appears to be in force-free conditions where $\alpha < 0.5$ surrounding the flux rope center. By contrast, the FR2 has a complex behavior that the most leading parts of the flux rope (including the crater region) seem not in the force-free conditions but the field draping region appears to be force-free.

4. Non-frozen-in Ion Behavior and deHoffmann-Teller Frame Analysis

Figures 8a–8c and 9a–9c show comparison of the measured electric fields [Lindqvist et al., 2016] with the convection electric fields $-\mathbf{V}_i \times \mathbf{B}$ and $-\mathbf{V}_e \times \mathbf{B}$ for FR1 and FR2, respectively. Overall, the $-\mathbf{V}_e \times \mathbf{B}$ fields more or less agree with the measured electric fields, albeit with small systematic constant offsets. But, the ion plasma appears not to be magnetized in some small portions of the flux rope, indicating that the non-frozen-in ion behavior is present [Eastwood et al., 2016].

Figures 8d and 9d show the measured electric fields versus the convection electric fields $-\mathbf{V}_{HT} \times \mathbf{B}$. Here \mathbf{V}_{HT} is the deHoffmann-Teller (HT) frame velocity [Khrabrov and Sonnerup, 1998]. In the HT frame reference, the electric field vanishes in the plasma, i.e., $\mathbf{E}' = \mathbf{E} + \mathbf{V}_{HT} \times \mathbf{B} = 0$. The existence of a good HT frame implies that the magnetic field structure is stationary and time-independent when viewed in that frame. A good HT frame has a correlation coefficient (CC) of ~ 1 between \mathbf{E} and $-\mathbf{V}_{HT} \times \mathbf{B}$. For FR1, $\mathbf{V}_{HT1} = (-23.6, 30.9, -218.3)$ km/s

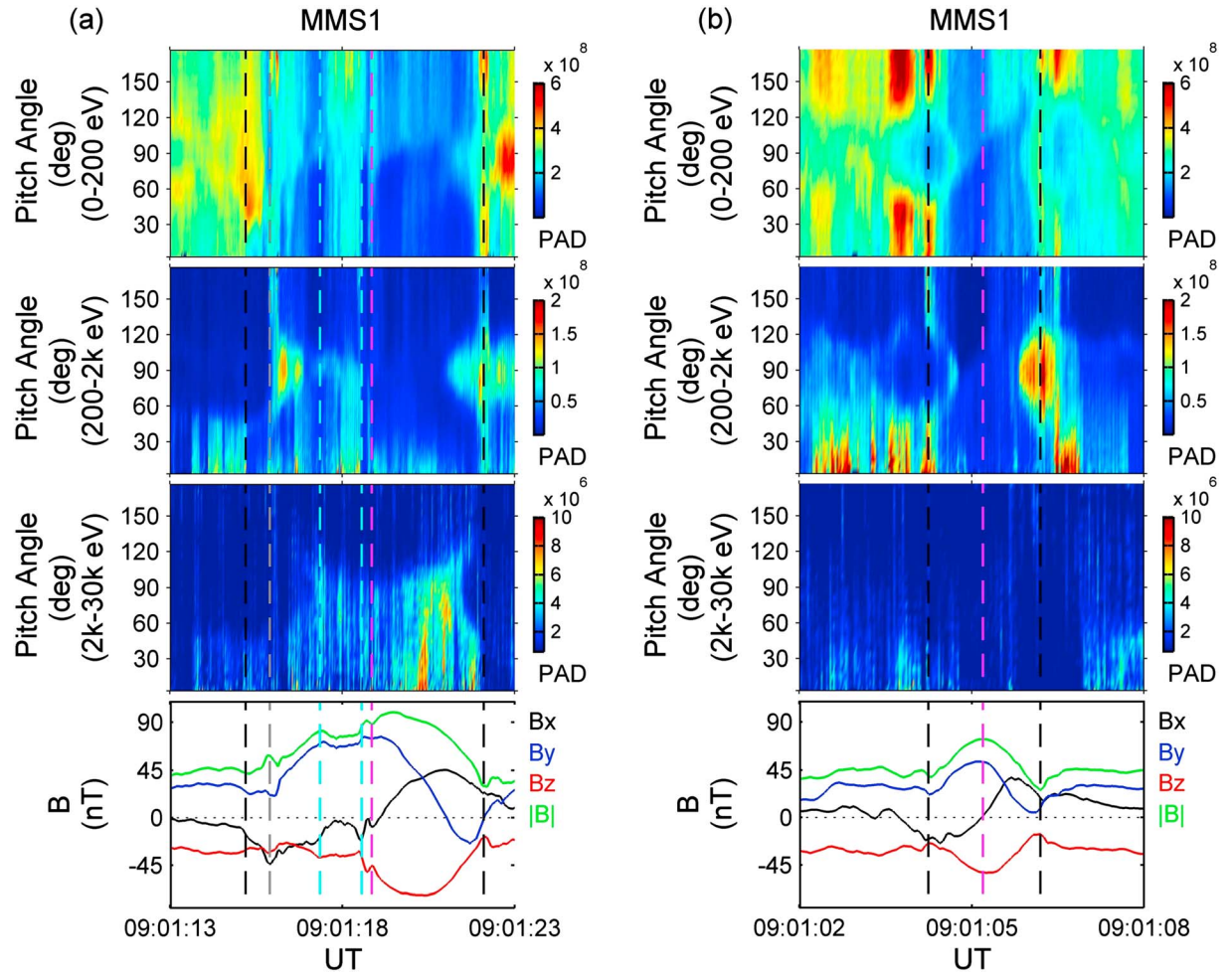


Figure 5. MMS1 observations of electron pitch angle distributions for three different energy ranges (0–200 eV, 200–2 k eV, and 2 k–30 k eV) for (a) FR2 and (b) FR1.

with $CC = 0.94$. For FR2, $\mathbf{V}_{HT2} = (-26.9, -17.4, -99.0)$ km/s with $CC = 0.75$. From the HT analysis results, it is concluded that the FR2 is time-dependent while the FR1 is in quasi-steady conditions.

5. Flux Rope Simulation

In this section we use the time-dependent, two-dimensional, ideal MHD equations to simulate the formation of the crater region and the B_x depression as observed within the FR2. The simulation scheme we use is the same as *Teh et al.* [2015]. At $t = 0$, the initial magnetic field and plasma profiles of a typical flux rope are implemented and expressed by the analytical flux rope model for magnetohydrostatic equilibrium, as shown by equations (3a)–(3d) in *Teh et al.* [2015]. The initial typical flux rope parameters used are $\varepsilon = 0.15$, $\kappa = 6.0$, $\gamma = 2.69$, $B_{x0}^2 = 0.7$, $B_{z0}^2 = 0.3$, $\beta_\infty = 0.1$, and $L_0 = 1.0$. Detailed descriptions for these parameters can be found in *Teh et al.* [2015]. To break the equilibrium state at $t = 0$, we impose transverse magnetic field perturbations into the system, which are expressed as

$$\tilde{b}_x = -2y(H_0/k)\cos(kx)e^{-2y^2} \quad (1)$$

$$\tilde{b}_y = (H_0/2)\sin(kx)e^{-2y^2} \quad (2)$$

Here H_0 is constant and $k = 1$. We use $H_0 = 0.1$ to induce the depression of the transverse magnetic fields. At later time t , we impose pressure perturbation into the system, which is expressed as

$$\tilde{p} = D_0 \operatorname{sech}^2[G_0\pi(x - x_0)/L_x]e^{-(y/0.4)^2} \quad (3)$$

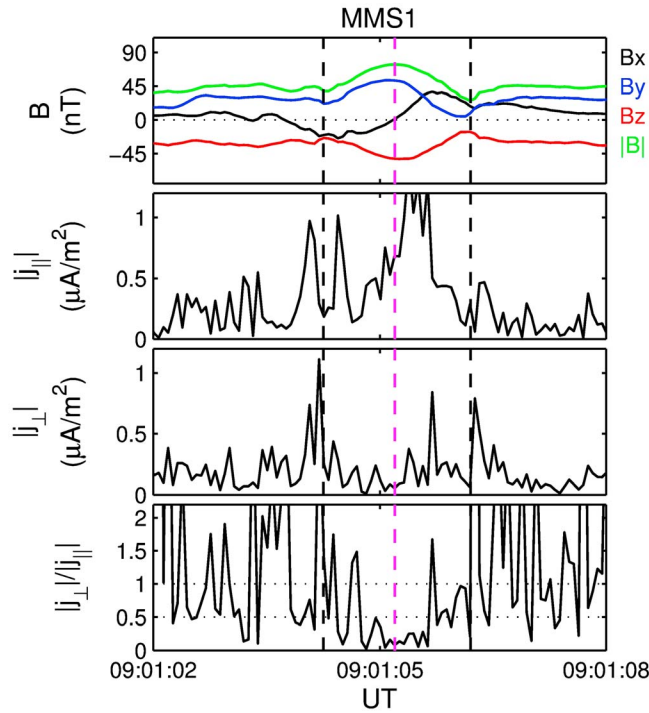


Figure 6. Parallel and perpendicular currents of FR1 calculated from MMS1 FPI data.

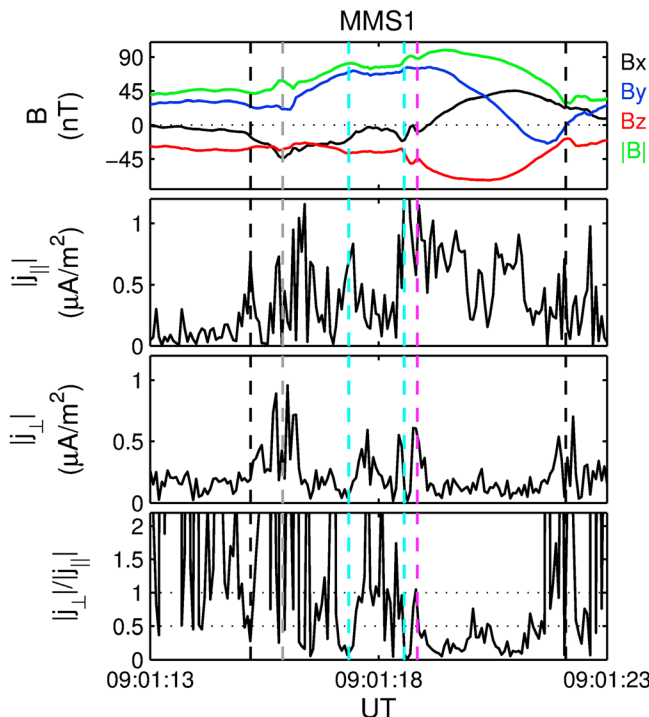


Figure 7. Parallel and perpendicular currents of FR2 calculated from MMS1 FPI data.

Here $D_0 = 0.15$, $G_0 = 8$, and $L_x = 2\pi$. Since the observed crater region is formed on the leading part of the flux rope, we therefore use $x_0 = -0.5$ instead of $x_0 = 0$. Note that the pressure perturbation will induce a density perturbation as $\tilde{n} = (1/\Gamma)(n/p)\tilde{p}$, where n and p are the values at time t , and $\Gamma = 5/3$. This induced density perturbation is analogous to the observation of the magnetosheath plasma streaming into the flux rope.

Figure 10 shows the magnetic field lines of a flux rope with the axial field B_z and thermal pressure P in color for time $t = 0$ and $t = 25$. Note that the field lines shown at $t = 0$ are not perturbed. Figure 11 shows the simulation data (B_y , B_z , n , P , P_b , and P_t) along the line $y = 0$ for different time steps. In Figure 11a, one can find that the normal field component B_y is depressed when the magnetic field perturbations are imposed at $t = 0$. After that, the B_y is not varied significantly. At $t = 5$, the B_z , n , P , P_b , and P_t are all decreasing as the flux rope is expanding along the x direction. At $t = 10$, the pressure perturbation is imposed at $x = -0.5$, as shown by the red line in Figure 11d. After that, a dip or crater is formed at $x = -0.5$ in the axial field B_z to sustain the force balance. Consequently, in the crater region the magnetic pressure is decreased while the thermal pressure and plasma density are increased, consistent with that observed by MMS. We note that the magnetic and thermal pressures within the crater are more or less in the quasi-steady state after $t = 15$, while the dip at $x = -0.5$ moves slightly to the left after $t = 25$ (not shown).

6. Summary and Discussion

We have examined the interior fine structures of two ion-scale magnetic flux ropes (FR1 and FR2) observed by MMS and have revealed that the FR2 is about 2 times larger in size than the FR1 ($\sim 5 d_i$) and the two flux

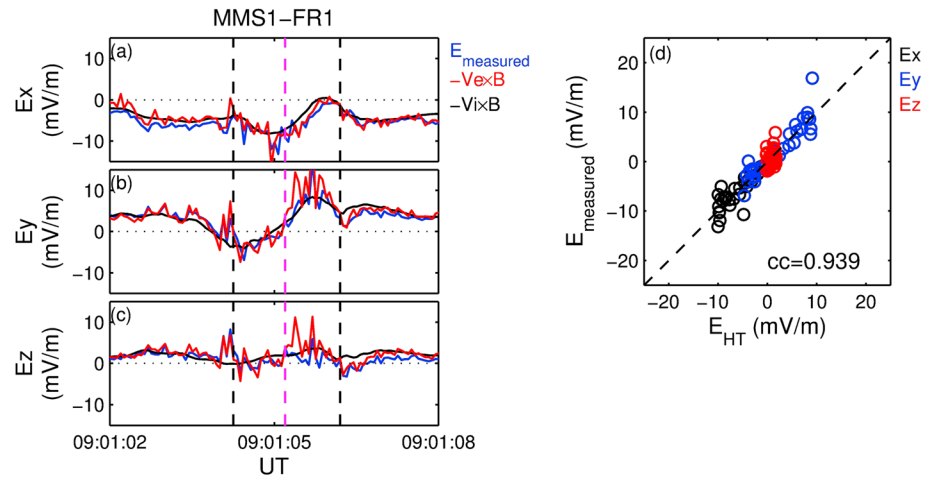


Figure 8. (a–c) Comparison of the measured electric fields with the $-\mathbf{V}_i \times \mathbf{B}$ and $-\mathbf{V}_e \times \mathbf{B}$ for FR1. (d) Plot of the measured electric fields versus the $-\mathbf{V}_{\text{HT}} \times \mathbf{B}$.

ropes are of non-frozen-in ion behavior. Some of their flux rope properties are contrasted. The electric current ratio j_{\perp}/j_{\parallel} indicates that the FR1 seems to be force-free while the FR2 appears not. The HT analysis reveals that the FR1 is in quasi-steady state while the FR2 is time-dependent. As a whole, we conclude that the FR1 is a quasi-steady, typical flux rope in the force-free conditions and the FR2 is a time-dependent, non-force-free flux rope. Additional findings have been discovered within the FR2, namely, (1) magnetic field draping and energetic electrons in the trailing part of the flux rope and (2) crater formation in the axial field and the magnetic pressure. The electron pitch angle distributions reveal that the one end of the FR2 could be connected to the Southern Hemisphere while the other one end could be open to the magnetosheath and that the magnetosheath plasma is streaming into the crater region along the field lines. We have performed the analytical flux rope simulation to demonstrate the formation of the crater region as observed within the FR2. A good agreement between the simulation results and the observations is achieved, indicating that the crater formation is due to the evolution of a typical flux rope to a crater-like one caused by the thermal pressure enhancement.

In the simulation, the flux rope evolves at $t=0$ due to the depression of the normal field component as observed. This field depression results in the expansion of the simulated flux rope, since the inward compression force $\mathbf{j}_z \times \mathbf{B}_{\perp}$ becomes weaker. Here \mathbf{j}_z is the axial electric current and \mathbf{B}_{\perp} is the transverse magnetic fields.

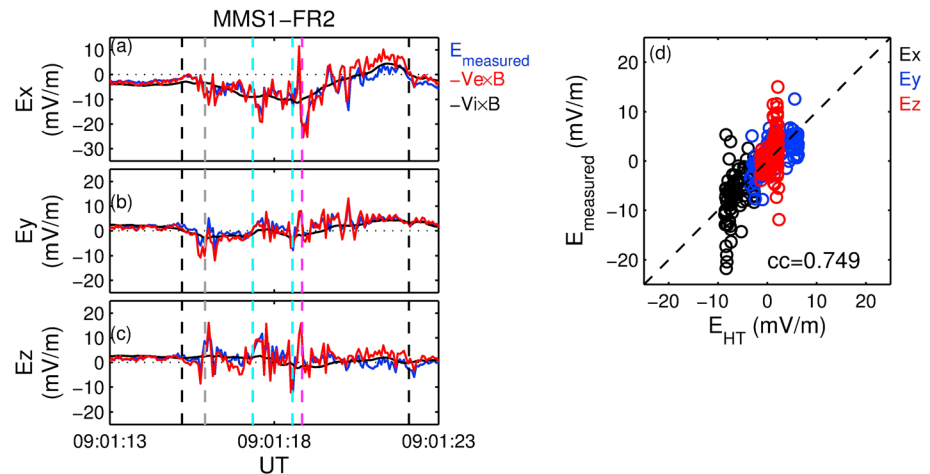


Figure 9. The same format as Figure 8 but for FR2.

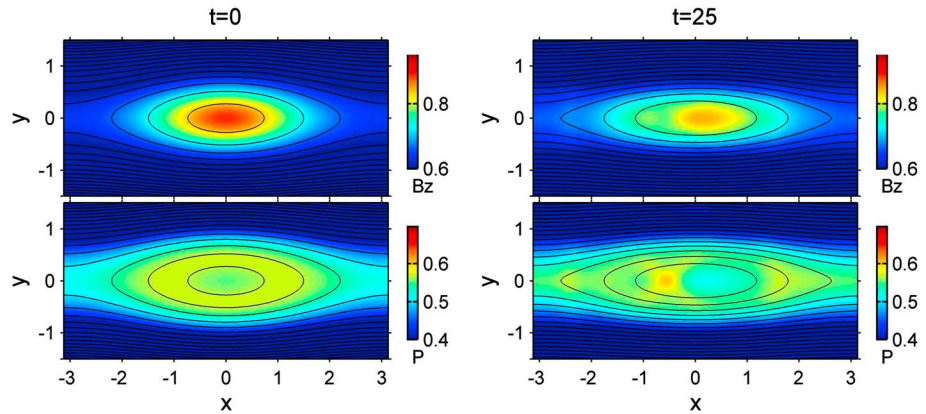


Figure 10. Magnetic field line map with the axial field B_z and the thermal pressure P in color for $t = 0$ and $t = 25$. The initial simulated flux rope is of a typical flux rope.

As a result, the magnetic and thermal pressures decrease during the expansion, as shown by the blue line ($t = 5$) in Figures 11d and 11e. In reality, such a pressure depression could induce a pressure gradient force along the field lines between the flux rope and the magnetosheath. It could be the reason why the magnetosheath plasma is feeding into the crater region along the field lines such that the thermal pressure is enhanced. We point out that the normal field component B_y does not vary significantly after $t = 5$, as shown in Figure 11a. Consequently, a large depression in B_y would not happen if the pressure perturbations were imposed at $t = 0$, instead of the magnetic field perturbations. The depression of the normal field component could be due to the changes of the field and plasma environment surrounding the flux rope. Further, it can be

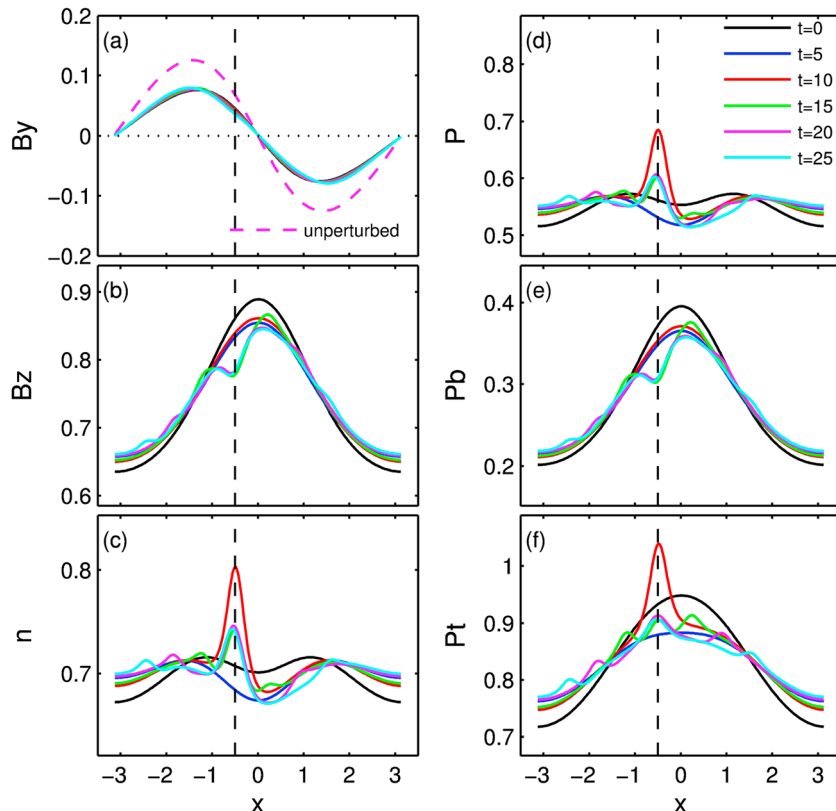


Figure 11. Simulation data along the line $y = 0$ for different time steps. Shown are the normal field component B_y , axial field B_z , plasma density n , thermal pressure P , magnetic pressure P_b , and total pressure P_t .

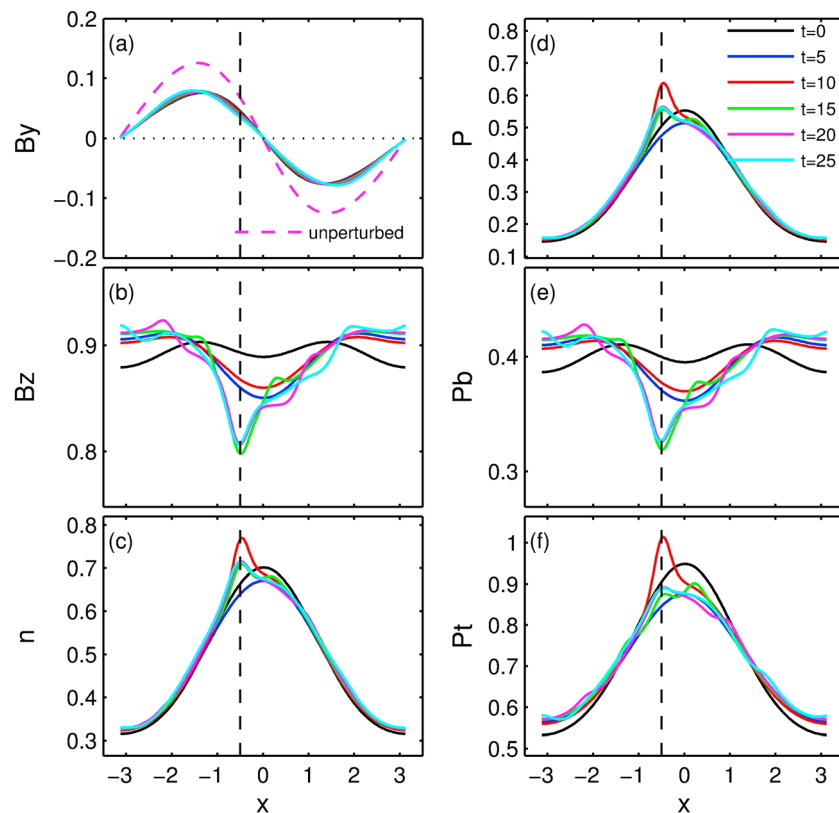


Figure 12. The same format as Figure 11 but for the simulation with a crater-like flux rope at $t = 0$.

found in Figure 7 that the non-force-free behavior ($j_{\perp}/j_{\parallel} > 1$) happens near the edge of the flux rope. These forces may result in the deformation of the flux rope.

According to the bipolar signature, the FR2 is seen by MMS1, 3, 2, and 4, in that order. The duration is ~ 0.4 s between the flux rope encounters by MMS1 and MMS4. The peaks of the ion thermal pressure within the crater seen by MMS1, 3, 2, and 4 are 1.49 nPa, 1.49 nPa, 1.66 nPa, and 1.52 nPa, respectively. Consider that this pressure variation is due to the entry of the magnetosheath plasma into the crater, it would then suggest that the FR2 is evolving/expanding in time, which is consistent with the HT analysis result that the FR2 is time-dependent.

In the present simulation study the Hall term is not included in the Ohm's law to describe the non-frozen-in ion behavior presented in some small portions of the flux rope. In spite of that, one can see that the ideal MHD simulation is able to reproduce the overall crater properties as observed. There is a rare feature that the crater region solely appears in the leading part of the flux rope. To our knowledge, this asymmetric feature is for the first time reported. Yet we are not clear how it is formed. Probably, it could be the consequence of the magnetic field draping effects.

We have also performed a flux rope simulation for a crater-like flux rope at $t = 0$, using the same perturbation parameters as previous. The simulation results are shown in Figure 12, the same format as Figure 11. It is found that a new crater region is being formed at $x = -0.5$. However, the overall profiles of the magnetic and thermal pressures are not in line with the observations. Therefore, it is indicated that the initial stage of the FR2 is of a typical flux rope as the FR1. We should point out that there is no crater-like flux rope in the equilibrium where the thermal pressure is lower at the flux rope center, because there is no outward expansion force at all to counter the inward compression force.

In conclusion, the evolution of a typical ion-scale flux rope is detected by the MMS spacecraft using the high time-resolution field and plasma measurements. A good agreement between the simulation and the observation demonstrates that the crater formation is resulted from the thermal pressure enhancement, which could be the consequence of the depression of the transverse magnetic fields.

Acknowledgments

This work was supported by the Fundamental Research Grant Scheme (FRGS) from the Ministry Education of Malaysia (FRGS/1/2016/STG02/UKM/03/1) and the Austrian Science Fund (FWF: I2016-N20). We are grateful for the dedicated efforts of the entire MMS mission team, including development, science operations, and the Science Data Center at the University of Colorado. The simulations were performed with resources at the Space Research Institute of Austrian Academy of Sciences. MMS data can be downloaded at <https://lasp.colorado.edu/mms/sdc/public/>. W.L.T. and T.K.M.N. will provide the simulation data used to generate the figures in the paper if requested.

References

- Burch, J. L., T. E. Moore, R. B. Torbert, and B. L. Giles (2016), Magnetospheric multiscale overview and science objectives, *Space Sci. Rev.*, **199**, 5–21, doi:10.1007/s11214-015-0164-9.
- Eastwood, J. P., et al. (2016), Ion-scale secondary flux ropes generated by magnetopause reconnection as resolved by MMS, *Geophys. Res. Lett.*, **43**, 4716–4724, doi:10.1002/2016GL068747.
- Farrugia, C. J., R. P. Rijnbeek, M. A. Saunders, D. J. Southwood, D. J. Rodgers, M. F. Smith, C. P. Chaloner, D. S. Hall, P. J. Christiansen, and L. J. C. Woolliscroft (1988), A multi-instrument study of flux transfer event structure, *J. Geophys. Res.*, **93**(14), 14,465–14,477, doi:10.1029/JA093iA12p14465.
- Farrugia, C. J., et al. (2016), Magnetospheric Multiscale Mission observations and non-force free modeling of a flux transfer event immersed in a super-Alfvénic flow, *Geophys. Res. Lett.*, **43**, 6070–6077, doi:10.1002/2016GL068758.
- Hwang, K.-J., et al. (2016), The substructure of a flux transfer event observed by the MMS spacecraft, *Geophys. Res. Lett.*, **43**, 9434–9443, doi:10.1002/2016GL070934.
- Khrabrov, A. V., and B. U. Ö. Sonnerup (1998), DeHoffmann-Teller analysis, in *Analysis Methods for Multi-Spacecraft Data*, edited by G. Paschmann and P. W. Daly, pp. 221–248, International Space Science Institute, Bern.
- Lindqvist, P.-A., et al. (2016), The spin-plane double probe electric field instrument for MMS, *Space Sci. Rev.*, **199**, 137–165, doi:10.1007/s11214-014-0116-9.
- Paschmann, G., G. Haerendel, I. Papamastorakis, N. Sckopke, S. J. Bame, J. T. Gosling, and C. T. Russell (1982), Plasma and magnetic field characteristics of magnetic flux transfer events, *J. Geophys. Res.*, **87**(A4), 2159–2168, doi:10.1029/JA087iA04p02159.
- Pollock, C., et al. (2016), Fast plasma investigation for magnetospheric multiscale, *Space Sci. Rev.*, **199**, 331–406, doi:10.1007/s11214-016-0245-4.
- Russell, C. T., et al. (2016), The magnetospheric multiscale magnetometers, *Space Sci. Rev.*, **199**, 189–256, doi:10.1007/s11214-014-0057-3.
- Schwartz, S. J. (1998), Shock and discontinuity normals, Mach numbers and related parameters, in *Analysis Methods for Multi-Spacecraft Data*, edited by G. Paschmann and P. W. Daly, pp. 249–270, International Space Science Institute, Bern.
- Teh, W.-L., R. Nakamura, H. Karimabadi, W. Baumjohann, and T. L. Zhang (2014), Correlation of core field polarity of magnetotail flux ropes with the IMF By: Reconnection guide field dependency, *J. Geophys. Res. Space Physics*, **119**, 2933–2944, doi:10.1002/2013JA019454.
- Teh, W.-L., T. K. M. Nakamura, R. Nakamura, W. Baumjohann, and M. Abdullah (2015), On the evolution of a magnetic flux rope: Two-dimensional MHD simulation results, *J. Geophys. Res. Space Physics*, **120**, 8547–8558, doi:10.1002/2015JA021619.
- Wang, R. S., Q. Lu, R. Nakamura, C. Huang, A. Du, F. Guo, W. Teh, M. Wu, S. Lu, and S. Wang (2016), Coalescence of magnetic flux ropes in the ion diffusion region of magnetic reconnection, *Nat. Phys.*, **12**, 263–267, doi:10.1038/nphys3578.
- Zhang, H., et al. (2010), Evidence that crater flux transfer events are initial stages of typical flux transfer events, *J. Geophys. Res.*, **115**, A08229, doi:10.1029/2009JA015013.
- Zhao, C., et al. (2016), Force balance at the magnetopause determined with MMS: Application to flux transfer events, *Geophys. Res. Lett.*, **43**, 11,941–11,947, doi:10.1002/2016GL071568.